CHARACTERIZATION OF NODULAR CAST-IRON USING MULTI-SCALE CONSTITUTIVE MODELING

Fernando D. Carazo[a], **Sebastián M. Giusti**[b], **Adrián D. Boccardo**[a], **Patricia M. Dardati** [a] **and Luis A. Godoy** [c]

[a]*Universidad Tecnológica Nacional - Facultad Regional Córdoba, CIII - Departamento de Ingeniería Mecánica. Maestro M. Lopéz esq. Cruz Roja Argentina, Ciudad Universitaria, Córdoba, Argentina, fcarazo@scdt.frc.utn.edu.ar, pdardati@industrial.frc.utn.edu.ar, aboccardo@mecanica.frc.utn.edu.ar, http://www.frc.utn.edu.ar*

[b]*Universidad Tecnológica Nacional - Facultad Regional Córdoba, Departamento de Ingeniería Civil , Maestro M. Lopéz esq. Cruz Roja Argentina, Ciudad Universitaria, Córdoba, Argentina - CONICET, sgiusti@civil.frc.utn.edu.ar, http://www.frc.utn.edu.ar*

[c]*Universidad Nacional de Córdoba, Facultad de Ciencias Exactas, Físicas y Naturales , Avenida Vélez Sársfield 1611, Córdoba, Argentina - CONICET, lgodoy@com.uncor.edu, http://www.efn.uncor.edu*

Keywords: Multi-scale modeling, Material characterization, Nodular cast-iron, Finite element, Representative volume element.

Abstract. The constitutive properties of cast-iron materials depend on the graphite morphology and the characteristics of the metallic matrix. Specifically, in the nodular cast-iron, these properties are affected by the spheroidicity of the graphite and the volume fractions of the ferritic phase and pearlitic microconstituent. The constitutive properties of such materials are usually presented by means of an analytical formula in terms of micro-structural characteristics. In the derivation of an analytical expression, the formulation of hypotheses are needed to define the behavior, shape and distribution of the elements in the micro-structure. Then, the analytical formulation to predict the constitutive behavior of the nodular cast-iron is restricted to the micro-structures that satisfy such hypotheses. In the present work, we use a computational constitutive multi-scale model to predict the Young's modulus of the pearlitic nodular cast-iron. In order to define an adequate Representative Volume Element, we use a set of micrographics images, obtained from an optical device. Each image is enhanced and segmented to obtain the volume fraction of each phase and the boundary of each object in the micrography. With this information, a finite element mesh is constructed for each image. Finally, the numerical results are compared with an analytical expression. Some conclusions are presented at the end of the work.

1 INTRODUCTION

Cast irons are a Fe-C-Si alloy with $3.0 - 4.3\%C$ and $1.3 - 3.0\%Si$, in which the high carbon content determines the mechanical properties based on the carbon retained in solid solution at room temperature, while silicon promotes the precipitation of carbon in the form of graphite. At present, cast irons are manufactured in larger quantities than any other type of cast alloy (Panchal, 2010), and in some cases they have replaced steel castings. This is mainly due to their lower melting point and high carbon content, which improves the castability and fluidity during the pouring process, achieving lower levels of defects produced during the filling of a mold, and reaching a wide range of properties based on the morphology of graphite and micro-constituents present in the matrix at room temperature (Table 2).

One of the products manufactured in large quantities by foundries is the nodular cast iron, also known as spheroidal or ductile cast iron, which represents 33% of the global production of ferrous alloys, and with the aluminum and magnesium castings has had a great rate of production in the last years (Spada et al., 2008). Nodular cast iron is an iron carbon-based alloy, in which carbon is present in the form of spheroidal graphite particles; this provides high values of tensile strength, elongation, impact, wear and fracture resistance due to the nodular shape of the graphite. Special properties such as: hardenability, corrosion resistance, high temperature resistance, resistance to thermal fatigue, and wear resistance, can be achieved by adding silicon and molybdenum.

The typical micro-structures of nodular cast iron (in as-cast condition) can be seen in the micrograph shown in Figure 1, in which the graphite nodules are surrounded by a ferrite envelope forming the characteristic "bull's-eye" of these ternary Fe-C-Si alloys. The rest of the matrix is formed by pearlite, which is a mixture of ferrite and cementite llamellar. In as-cast condition, the nodular cast iron can be classified depending on the metallic matrix in (see Table 1): ferritic, mostly ferritic, ferritic-pearlitic, mostly perlitic and martensitic. Interest in obtaining a matrix like those mentioned above is due to the wide range of mechanical properties that can be achieved with a nodular cast iron in as-cast conditions without further heat treatment. According to what type of matrix is obtained, properties such as tensile strength, yield strength and hardness can be improved by increasing the volume fraction of pearlite but this reduces the elongation and ductility. On the other hand, the fracture toughness, wear resistance and dynamic properties improve as the volume fraction of ferrite increases but this reduces the tensile strength, yield strength and hardness.

Grade	Description	Industrial applications
$60 - 40 - 18$	Ferritic can be annealed	Impact resistant parts at low temperatures
$65 - 45 - 12$	Mostly ferritic casting or annealed	General Service
$80 - 55 - 06$	Ferritic-pearlitic can be normalized	General Service
$100 - 70 - 03$	Mostly pearlitic can be normalized	The best combination of strength and toughness
$120 - 70 - 02$	Martensitic oil hardening and tempered	High toughness and wear resistance

Table 1: Grades of nodular cast irons according to ASTM A536.
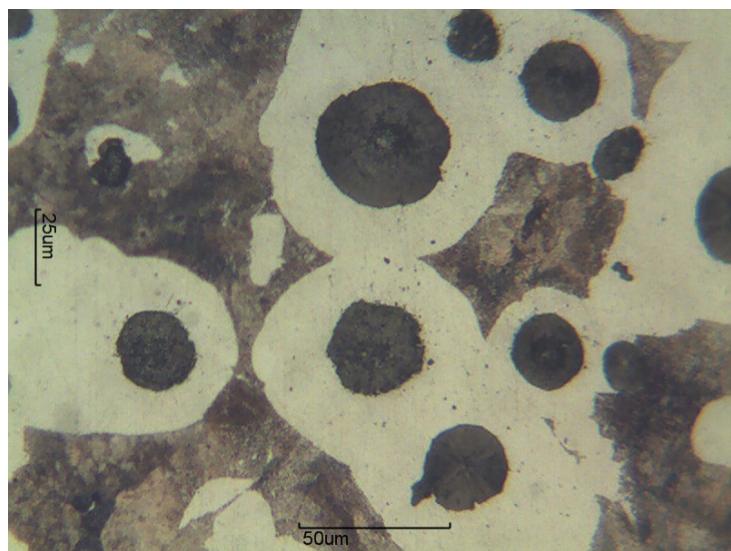
Figure 1: Typical micro-structure of semi-pearlitic (ferritic) nodular cast iron.

Grade	Tensile Strength (MPa)	Yield Strength (MPa)	Hardness	Elongation (%)
$60 - 40 - 18$	42000	28000	$149 - 187$	18
$65 - 45 - 12$	45000	32000	$170 - 207$	12
$80 - 55 - 06$	56000	38000	$187 - 255$	6
$100 - 70 - 03$	70000	47000	$217 - 267$	3
$120 - 70 - 02$	84000	63000	$240 - 300$	2

Table 2: Mechanical properties of different grades according to ASTM A536.

The mechanical properties of nodular cast iron vary in a wide range of values (as shown in Table 2), mostly controlled by two factors: *(a)* Type, size and distribution of graphite nodules; and *(b)* Type of matrix and defects present: ferrite/pearlite relation, its own characteristic and the presence of micro-structural defects.

The size and distribution of graphite nodules depend on the composition of the melt and inoculation treatment. A good melt treatment promotes graphite nodules type I (ASTM A247); whereas, a good inoculation treatment favors nodules type A (random distribution and orientation) and nodules size class 1 (ASTM A247). The most widely used element for the production of spheroidal graphite is magnesium. The amount of residual magnesium required to produce spheroidal graphite is about $0.03 - 0.05\%Mg$. The adequate content of magnesium depends of the cooling rate: for higher cooling rate the nodular cast iron requires less magnesium, other factor that affect the magnesium that can be added is the initial sulfur content in the molten, if the residual magnesium content is lower than those required, the nodularity is inadequate, which results in a deterioration of the mechanical properties of the nodular cast iron. For magnesium contents higher than required, carbides are promoted, which weakens the casting. Finally, the phosphorus and sulfur are the less important elements present in cast irons, but more than 0.15% of these elements promotes low quality of spheroidal graphite, so their amounts must be considerably less.

The type of matrix depends on the cooling rates and chemical composition, which can alter the ferrite and pearlite contents, size and distribution; the most important feature of ferrite is the grain size. On the other hand, the most important features of pearlite micro-constituents are:

interlamellar spacing, colonies and nodules sizes. The manganese and copper content vary as a function of the desired matrix: typically, manganese content must be lower than 0.1% to obtain a ferritic matrix and larger than 0.9% to produce a pearlitic matrix, similar trends occur with copper. Also, higher cooling rates promote the so called chilled iron; in this case, the excess carbon is found in the form of massive carbides. Intermediate cooling rates promote the so-called mottled iron, in which carbon is present in the form of iron carbide and graphite. Finally, adequate and slow cooling rate produce nodular graphite embedded in a ferrite/pearlite matrix.

In cast alloys the mechanical properties also depend on the presence of micro-porosities, micro-inclusions, micro-segregations, carbides, and second phase particles. Microstructural factors that contribute to a loss of toughness are: reduction in percent nodularity (related to the quantity of degenerated graphite), high percentage or continuity of intercellular or interdendritic carbides and micro-porosity.

The goal of the metallurgist is to design a process producing a structure which yields the expected mechanical properties. This requires knowledge of the relations between structure and mechanical properties in alloys as well as identification of the factors affecting the structure.

This paper presents a computational constitutive multi-scale model to predict elastic constants such as Young's modulus and Poisson ratio of a pearlitic nodular cast-iron by taking into account the influence of graphite and matrix volumetric phase fractions and nodularity of samples used in the study. Numerical values are compared with results obtained from an analytical formula extracted from Mazilu and Ondracek (1990).

2   LITERATURE REVIEW

As discussed above, in the as-cast condition the micro-structure in nodular cast iron is formed by graphite nodules embedded in a mixture of ferrite and pearlite matrix (Figure 1); and its mechanical properties strongly depend on the nodularity, amount and distribution of ferrite grains and amount, interlamellar spacing and size of pearlite colonies (Table 2). Most papers study the micro-structural/mechanical properties relation for models which are based on a phenomenological point of view based on experiments. Wenzhen and Baicheng (1996) developed a model for the nucleation and growth of the micro-structure evolution in nodular cast iron from solidification at room temperature and applied this model to predict cooling curves, micro-structures and mechanical properties of a nodular cast iron crankshaft. To predict the mechanical properties, they employed experimental expressions developed by Lundback et al. (1988). They compute the Brinell hardness proposing a linear relationship between this and pearlite volume fraction and then they calculate the tensile strength, yield strength and elongation as a function of Brinell hardness. Guo et al. (1997) proposed a relation to characterize Brinell hardness, tensile strength, yield strength and elongation taking into account characteristics of the graphite and metallic matrix. They also discussed the influence of graphite nodule count, nodularity, fraction of graphite, ferrite and pearlite on the fracture mechanism context. Venugopalan and Alagarsamy (1990) obtained a regression equation for the as-cast fraction of ferrite in the matrix in order to evaluate the quantitative effects of alloying elements on the microstructure. The equation is a linear multiple regression with second order terms included to account for synergistic effect of molybdenum with nickel and cooper. The composite matrix micro-hardness is next calculated by the rule of mixture as a function of ferrite and pearlite micro-hardness and volume fractions. Finally, they computed the tensile and yield strength as a function of micro-hardness. Yu and Loper Jr. (1988) studied the effect of alloying elements on hardenability of pearlitic and martensitic nodular cast iron. The effect of molybdenum, copper and nickel in forming ferrite in a variety nodular cast iron sections was evaluated by using linear analytics

regression and obtained the equation for ferrite and Brinell hardness. For casting having more than 90% of pearlite, they proposed another expression to compute the Brinell hardness which varies exponentially as a function of volume pearlite fraction. Svensson et al. (1993) studied the influence of silicon content and its relation with mechanical properties of nodular cast irons with different contents of this element. From an experimental point of view, they propose three equations to predict the ferrite and pearlite micro-hardness, and Brinell hardness as a function of ferrite and pearlite volumetric fractions and micro-hardness calculated using a mixture rule. The expressions developed are valid in the interval of $1.7 - 4.9\%Si$.

The researchers mentioned above considered the influence of the alloying elements (chemical composition) and section size (cooling rate) of castings on the mechanical properties, and their methodologies are used because they involve knowledge of just a few variables and lead to good practical results under limited conditions of applications; however, they can not be applied to all cases and lack generality.

There are also models that predict the constitutive properties of a casting according to their micro-structural features based on multi-scale modeling and continuum micromechenics. Boccaccini (1997), appled an analytical formulation previously developed by Mazilu and Ondracek (1990) to study the influence of the shape and volume fraction of graphite nodules in Young's modulus. In this paper, Boccaccini takes into account: graphite volume fraction, matrix and graphite's Young modulus, the ratio between the length and width of the ellipsoid (commonly referred to as ellipsoidal aspect ratio EAR), and the direction of the applied stress and the rotational axis of the spheroids. Pundale et al. (2000) predicted the effective Young's modulus of nodular cast iron by assuming symmetry in a unit-cell model in plane stress and axisymmetric formulations. They investigated the influence of graphite volume fraction, shape, size and distribution of graphite assuming nodules as voids. They proposed a model to study the influence of surface irregularities on the Young's modulus. Wolfgang et al. (2003) proposed a self-consistent $3D$ unit cell model to simulate the effect of graphite aspect ratio on the elastic constant of nodular cast iron. In their simulation they employed the cube shaped unit-cell, which is made up of an inner rotational ellipsoid of graphite surrounded by ferritic nodular cast iron in a concentric outer ellipsoid of the same aspect ratio as the inner graphite ellipsoid. In order to obtain elastic properties the unit cell was subjected to uniaxial loading. Calculations of stress and strain distribution for different ellipsoid's orientation were carried out by the finite element method. Finally, when the iterative process converges, they calculate Young's modulus and Poisson's ratio from Hooke's law. Collini and Nicoletto (2005) proposed a unit-cell model to predict the constitutive law and failure of ferritic/pearlitic nodular cast iron. This continuum and numerical approaches were developed within the framework of continuum mechanics and finite element methods respectively. These authors investigated the effect of some micro-structural features, such as graphite volume fraction and ferrite/pearlite ratio of the metallic matrix on the mechanical properties of nodular cast iron and they compared numerical results with previous experimental work. Nicoletto et al. (2006) considered the influence of the ferrite/pearlite ratio on the mechanical properties in nodular cast iron for three different micro-structures characterized using metallographic methodology, then micro-mechanics models based on unit-cell approach and the finite element method were developed to describe the constitutive response and to predict the behavior of the alloys.

From the papers reviewed, only Wolfgang et al. (2003) characterized nodular cast iron using multi-scale modeling to determine the Young's modulus and Poisson coefficient in ferritic nodular cast iron using a unit-cell approach, while others authors determine the mechanical behavior of nodular cast irons under different conditions. In this paper the study of Wolfgang

et al. (2003) is extended by using a representative volume element in the simulations obtained in samples processed from different positions of 1-in. Y-block of pearlitic nodular cast iron. The computations are based on a variational framework that is subsequently solved by the finite element method.

3   MULTISCALE MODELING

This section presents a summary of the multi-scale constitutive theory upon which we rely for the estimation of the macroscopic elasticity properties. This family of (now well established) constitutive theories has been formally presented in a rather general setting by Germain et al. (1983) and later explored, among others, by Michel et al. (1999) and Miehe et al. (1999) in the computational context. When applied to the modeling of linearly elastic periodic media, it coincides with the asymptotic expansion-based theory described by Bensoussan et al. (1978) and Sanchez-Palencia (1980).

The starting point of this family of constitutive theories is the assumption that any point x of the macroscopic continuum (refer to Fig. 2) is associated to a local Representative Volume Ele-
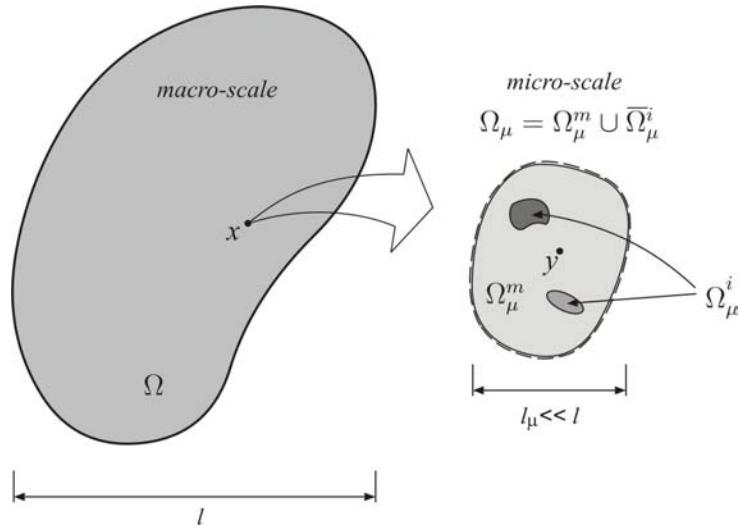

Figure 2: Macroscopic continuum with a locally RVE.

ment (RVE) whose domain Ω_μ, with boundary $\partial\Omega_\mu$, has characteristic length l_μ, much smaller than the characteristic length l of the macro- continuum domain, Ω. For simplicity, we consider that the RVE domain consists of a matrix, Ω_μ^m, containing inclusions of different materials occupying a domain Ω_μ^i (see Fig.2).

An axiomatic variational framework for this family of constitutive theories is presented in detail by de Souza Neto and Feijóo (2006). Accordingly, the entire theory can be derived from five basic principles: (1) The strain averaging relation; (2) A simple further constraint upon the possible functional sets of cinematically admissible displacement fields of the RVE; (3) The equilibrium of the RVE; (4) The stress averaging relation; (5) The Hill-Mandel Principle of Macro-Homogeneity, which ensures the energy consistency between the so-called micro- and macro-scales of the material. These are briefly stated in the following.

The first basic axiom – the strain averaging relation – states that the macroscopic strain tensor $\mathbf{E}$ at a point x of the macroscopic continuum is the volume average of its microscopic

counterpart $\mathbf{E}_\mu$ over the domain of the RVE:

$$\mathbf{E} := \frac{1}{V_\mu} \int_{\Omega_\mu} \mathbf{E}_\mu, \tag{1}$$

where V_μ is a total volume of the RVE and

$$\mathbf{E}_\mu := \nabla^s \mathbf{u}_\mu, \tag{2}$$

with $\mathbf{u}_\mu$ denoting the microscopic displacement field of the RVE. Equivalently, in terms of RVE boundary displacements, the homogenized strain (1,2) can be written as

$$\mathbf{E} = \frac{1}{V_\mu} \int_{\partial\Omega_\mu} \mathbf{u}_\mu \otimes_s \mathbf{n}, \tag{3}$$

where $\mathbf{n}$ is the outward unit normal to the boundary $\partial\Omega_\mu$ and $\otimes_s$ denotes the symmetric tensor product.

As a result of axiom (1) and, in addition, by requiring without loss of generality that the volume average of the microscopic displacement field coincides with the macroscopic displacement $\mathbf{u}$, any chosen set $\mathcal{K}_\mu$ of admissible displacement fields of the RVE must satisfy

$$\mathcal{K}_\mu \subset \mathcal{K}_\mu^* := \left\{ \boldsymbol{v} \in \left[H^1(\Omega_\mu)\right]^2 : \int_{\Omega_\mu} \boldsymbol{v} = V_\mu \mathbf{u} \,,\, \int_{\partial\Omega_\mu} \boldsymbol{v} \otimes_s \mathbf{n} = V_\mu \mathbf{E},\, [\![\boldsymbol{v}]\!] = \mathbf{0} \text{ on } \partial\Omega_\mu^i \right\}, \tag{4}$$

where $\mathcal{K}_\mu^*$ is the *minimally constrained set of cinematically admissible RVE displacement fields* and $[\![\boldsymbol{v}]\!]$ denotes the *jump* of function $\boldsymbol{v}$ across the matrix/inclusion interface $\partial\Omega_\mu^i$, defined as

$$[\![(\cdot)]\!] := (\cdot)|_m - (\cdot)|_i, \tag{5}$$

with subscripts m and i associated, respectively, with quantity values on the matrix and inclusion. Now, without loss of generality, $\mathbf{u}_\mu$ may be decomposed as a sum

$$\mathbf{u}_\mu (\boldsymbol{y}) = \mathbf{u} + \bar{\mathbf{u}} (\boldsymbol{y}) + \tilde{\mathbf{u}}_\mu (\boldsymbol{y}), \tag{6}$$

of a constant (rigid) RVE displacement coinciding with the macro displacement $\mathbf{u}$, a field $\bar{\mathbf{u}} (\boldsymbol{y}) := \mathbf{E}\,\boldsymbol{y}$, linear in the local RVE coordinate $\boldsymbol{y}$ (whose origin is assumed without loss of generality to be located at the centroid of the RVE) and a fluctuation displacement field $\tilde{\mathbf{u}}_\mu(\boldsymbol{y})$ that, in general, varies with $\boldsymbol{y}$. With the above split, the microscopic strain field (2) can be written as a sum

$$\mathbf{E}_\mu = \mathbf{E} + \tilde{\mathbf{E}}_\mu, \tag{7}$$

of a homogeneous strain (uniform over the RVE) coinciding with the macroscopic strain and a field $\tilde{\mathbf{E}}_\mu := \nabla^s \tilde{\mathbf{u}}$ corresponding to a fluctuation of the microscopic strain about the homogenized (average) value.

The additive split (6) allows the constraint (4) to be expressed in terms of displacement fluctuations alone. It is equivalent to requiring that the (as yet to be defined) set $\tilde{\mathcal{K}}_\mu$ of admissible displacement fluctuations of the RVE be a subset of the *minimally constrained space of displacement fluctuations*, $\tilde{\mathcal{K}}_\mu^*$:

$$\tilde{\mathcal{K}}_\mu \subset \tilde{\mathcal{K}}_\mu^* := \left\{ \boldsymbol{v} \in \left[H^1(\Omega_\mu)\right]^2 : \int_{\Omega_\mu} \boldsymbol{v} = \mathbf{0}, \int_{\partial\Omega_\mu} \boldsymbol{v} \otimes_s \mathbf{n} = \mathbf{0},\, [\![\boldsymbol{v}]\!] = \mathbf{0} \text{ on } \partial\Omega_\mu^i \right\}. \tag{8}$$

At this point we introduce the further assumption that $\tilde{\mathcal{K}}_\mu$ is a *subspace* of $\tilde{\mathcal{K}}_\mu^*$. Then, we have that the space of *virtual displacement* of the RVE, defined as

$$\mathcal{V}_\mu := \left\{ \boldsymbol{\eta} \in \left[H^1(\Omega_\mu) \right]^2 : \boldsymbol{\eta} = \boldsymbol{v}_1 - \boldsymbol{v}_2; \ \forall \boldsymbol{v}_1, \boldsymbol{v}_2 \in \mathcal{K}_\mu \right\}, \tag{9}$$

coincides with the space of microscopic displacement fluctuations, i.e.,

$$\mathcal{V}_\mu = \tilde{\mathcal{K}}_\mu. \tag{10}$$

The next axiom establishes that the macroscopic stress tensor $\mathbf{T}$ is given by the volume average of the microscopic stress field $\mathbf{T}_\mu$ over the RVE, i.e.,

$$\mathbf{T} := \frac{1}{V_\mu} \int_{\Omega_\mu} \mathbf{T}_\mu. \tag{11}$$

The present paper is focused on RVEs whose matrix and inclusion materials are described by the classical isotropic linear elastic constitutive law. That is, the microscopic stress tensor field $\mathbf{T}_\mu$ satisfies

$$\mathbf{T}_\mu = \mathbb{C}_\mu \mathbf{E}_\mu, \tag{12}$$

where $\mathbb{C}_\mu$ is the fourth order isotropic elasticity tensor:

$$\mathbb{C}_\mu = \frac{E}{1 - \nu^2} \left[(1 - \nu)\, \mathbb{I} + \nu\, (\mathbf{I} \otimes \mathbf{I}) \right], \tag{13}$$

with E and ν denoting, respectively, the Young's modulus and the Poisson's ratio. These parameters are given by

$$E := \begin{cases} E_m & \text{if } \boldsymbol{y} \in \Omega_\mu^m \\ E_i & \text{if } \boldsymbol{y} \in \Omega_\mu^i \end{cases} \quad \text{and} \quad \nu := \begin{cases} \nu_m & \text{if } \boldsymbol{y} \in \Omega_\mu^m \\ \nu_i & \text{if } \boldsymbol{y} \in \Omega_\mu^i \end{cases}. \tag{14}$$

The parameters E_i and ν_i constant within each inclusion but may in general vary from inclusion to inclusion. In eq.(13), we use $\mathbf{I}$ and $\mathbb{I}$ to denote the second and fourth order identity tensors, respectively.

The linearity of (12) together with the additive decomposition (7) allows the microscopic stress field to be split as

$$\mathbf{T}_\mu = \bar{\mathbf{T}}_\mu + \tilde{\mathbf{T}}_\mu, \tag{15}$$

where $\bar{\mathbf{T}}_\mu$ is the stress field associated with the uniform strain induced by $\bar{\mathbf{u}}\,(\boldsymbol{y})$, i.e., $\bar{\mathbf{T}}_\mu = \mathbb{C}_\mu \mathbf{E}$, and $\tilde{\mathbf{T}}_\mu$ is the stress fluctuation field associated with $\tilde{\mathbf{u}}_\mu\,(\boldsymbol{y})$, i.e., $\tilde{\mathbf{T}}_\mu = \mathbb{C}_\mu \tilde{\mathbf{E}}$.

A further axiom of the theory is the so-called Hill-Mandel Principle of Macro-Homogeneity (Hill (1965) and Mandel (1971)). This principle establishes that the power of the macroscopic stress tensor at an arbitrary point of the macro-continuum must equal the volume average of the power of the microscopic stress over the RVE associated with that point for any cinematically admissible motion of the RVE. As a consequence of this principle the RVE body force $\mathbf{b}_\mu$ and external traction field $\mathbf{q}_\mu$ produce no virtual work (de Souza Neto and Feijóo (2006)):

$$\int_{\Omega_\mu} \mathbf{b}_\mu \cdot \boldsymbol{\eta} = 0 \quad \text{and} \quad \int_{\partial\Omega_\mu} \mathbf{q}_\mu \cdot \boldsymbol{\eta} = 0 \quad \forall \boldsymbol{\eta} \in \mathcal{V}_\mu. \tag{16}$$

That is, the RVE body force and external traction fields belong to the functional space orthogonal to the chosen $\mathcal{V}_\mu$ – they are reactions to the constraints imposed upon the possible displacement fields of the RVE.

The general theory is completed by a final axiom which establishes that the RVE must satisfy equilibrium. Then, with the introduction of (15) and (16) into the classical virtual work variational equation, we have that the *RVE mechanical equilibrium problem* consists of finding, for a given macroscopic strain $\mathbf{E}$, a cinematically admissible microscopic displacement fluctuation field $\tilde{\mathbf{u}}_\mu \in \mathcal{V}_\mu$, such that

$$\int_{\Omega_\mu} \tilde{\mathbf{T}}_\mu \cdot \nabla^s \boldsymbol{\eta} = - \int_{\Omega_\mu} \bar{\mathbf{T}}_\mu \cdot \nabla^s \boldsymbol{\eta} \quad \forall \boldsymbol{\eta} \in \mathcal{V}_\mu. \tag{17}$$

3.1 Classes of multi-scale constitutive models

The characterization of a multi-scale model of the present type is completed with the choice of a suitable space of cinematically admissible displacement fluctuations $\mathcal{V}_\mu \subset \tilde{\mathcal{K}}_\mu^*$. We list below the four classical possible choices:

- *Homogeneous strain model or Taylor model*. For this class of models the choice is

$$\mathcal{V}_\mu = \mathcal{V}_\mu^{\mathcal{L}} := \left\{ \tilde{\mathbf{u}}_\mu \in \tilde{\mathcal{K}}_\mu^* : \tilde{\mathbf{u}}_\mu(\boldsymbol{y}) = \mathbf{0} \,\forall \boldsymbol{y} \in \partial\Omega_\mu \right\}. \tag{18}$$

  The only possible reactive body force over Ω_μ orthogonal to $\mathcal{V}_\mu^{\mathcal{L}}$ is $\mathbf{b}_\mu = \mathbf{0}$. On $\partial\Omega_\mu$, the resulting reactive external traction, $\mathbf{q}_\mu \in \left(\mathcal{V}_\mu^{\mathcal{L}}\right)^\perp$, may be any function.

- *Linear boundary displacement model*. For this class of models the choice is

$$\mathcal{V}_\mu = \mathcal{V}_\mu^{\mathcal{L}} := \left\{ \tilde{\mathbf{u}}_\mu \in \tilde{\mathcal{K}}_\mu^* : \tilde{\mathbf{u}}_\mu(\boldsymbol{y}) = \mathbf{0} \,\forall \boldsymbol{y} \in \partial\Omega_\mu \right\}. \tag{19}$$

  The only possible reactive body force over Ω_μ orthogonal to $\mathcal{V}_\mu^{\mathcal{L}}$ is $\mathbf{b}_\mu = \mathbf{0}$. On $\partial\Omega_\mu$, the resulting reactive external traction, $\mathbf{q}_\mu \in \left(\mathcal{V}_\mu^{\mathcal{L}}\right)^\perp$, may be any function.

- *Periodic boundary fluctuations model*. This class of models is typical of the analysis of periodic media, where the macroscopic continuum is generated by the repetition of the RVE. In this case, the geometry of the RVE must satisfy certain geometrical constraints not needed by the other two classes discussed here. Considering for simplicity the case of polygonal RVE geometries (see fig.3), we have that the boundary $\partial\Omega_\mu$ is composed of a number of pairs of equally-sized subsets $\{\Gamma_i^+, \Gamma_i^-\}$ with normals $\mathbf{n}_i^+ = -\mathbf{n}_i^-$. For each pair $\{\Gamma_i^+, \Gamma_i^-\}$ of sides there is a one-to-one correspondence between points $\boldsymbol{y}^+ \in \Gamma_i^+$ and $\boldsymbol{y}^- \in \Gamma_i^-$.

  The periodicity of the structure requires that the displacement fluctuation at any point $\boldsymbol{y}^+$ coincide with that of the corresponding point $\boldsymbol{y}^-$. Hence, the space of displacement fluctuations is defined as

$$\mathcal{V}_\mu = \mathcal{V}_\mu^{\mathcal{P}} := \left\{ \tilde{\mathbf{u}}_\mu \in \tilde{\mathcal{K}}_\mu^* : \tilde{\mathbf{u}}_\mu(\boldsymbol{y}^+) = \tilde{\mathbf{u}}_\mu(\boldsymbol{y}^-) \,\forall \, \text{pairs} \, (\boldsymbol{y}^+, \boldsymbol{y}^-) \in \partial\Omega_\mu \right\}. \tag{20}$$

  Again, only the zero body force field is orthogonal to the chosen space of fluctuations. The reactive external surface traction fields that comply with the second of (16) are *anti-periodic*, i.e.,

$$\mathbf{q}_\mu(\boldsymbol{y}^+) = -\mathbf{q}_\mu(\boldsymbol{y}^-) \quad \forall \, \text{pairs} \, (\boldsymbol{y}^+, \boldsymbol{y}^-) \in \partial\Omega_\mu. \tag{21}$$
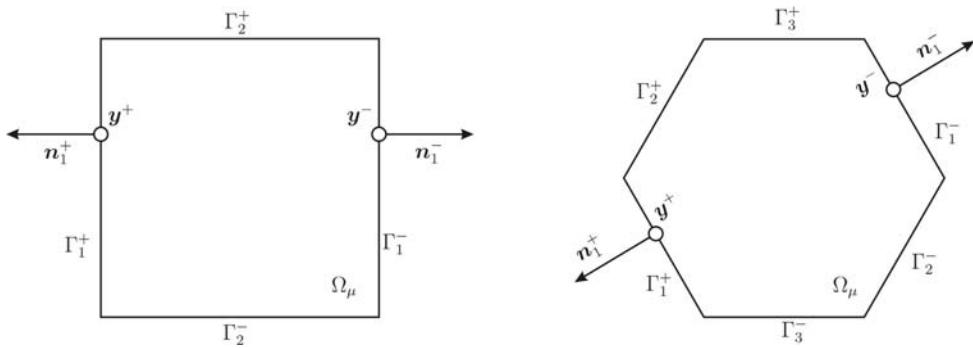
Figure 3: Typical RVE geometries for periodic media.

- *Minimally constrained* or *Uniform RVE boundary traction model*. In this case, we chose,

$$\mathcal{V}_\mu = \mathcal{V}_\mu^{\mathcal{U}} := \tilde{\mathcal{K}}_\mu^*. \tag{22}$$

Again only the zero body force field is orthogonal to the chosen space. The boundary traction orthogonal to the space of fluctuations satisfies the *uniform boundary traction condition* (de Souza Neto and Feijóo (2006)):

$$\mathbf{q}_\mu(\boldsymbol{y}) = \mathbf{T}\mathbf{n}(\boldsymbol{y}) \quad \forall \boldsymbol{y} \in \partial\Omega_\mu, \tag{23}$$

where $\mathbf{T}$ is the macroscopic stress tensor defined in (11).

3.2 The homogenized elasticity tensor

The assumed type of the material response in the microscale implies that the macroscopic response is linear elastic. That is, there is a *homogenized elasticity tensor* $\mathbb{C}$ such that

$$\mathbf{T} = \mathbb{C}\,\mathbf{E}. \tag{24}$$

A closed form for the homogenized constitutive tensor can be derived by the approach suggested by Michel et al. (1999) and relies on the representation of the RVE equilibrium problem (17) as a superposition of linear variational problems associated with the cartesian components of the macroscopic strain tensor. The resulting expression for $\mathbb{C}$ reads

$$\mathbb{C} = \bar{\mathbb{C}} + \tilde{\mathbb{C}}, \tag{25}$$

where $\bar{\mathbb{C}}$ is the volume average macroscopic elasticity tensor

$$\bar{\mathbb{C}} = \frac{1}{V_\mu} \int_{\Omega_\mu} \mathbb{C}_\mu, \tag{26}$$

and the contribution $\tilde{\mathbb{C}}$ (generally dependent upon the choice of space $\mathcal{V}_\mu$) is defined as

$$\tilde{\mathbb{C}} := \left[\frac{1}{V_\mu} \int_{\Omega_\mu} (\tilde{\mathbf{T}}_{\mu_{kl}})_{ij} \right] (\mathbf{e}_i \otimes \mathbf{e}_j \otimes \mathbf{e}_k \otimes \mathbf{e}_l), \tag{27}$$

where $\tilde{\mathbf{T}}_{\mu_{ij}} = \mathbb{C}_\mu \nabla^s \tilde{\mathbf{u}}_{\mu_{ij}}$ is the fluctuation stress field associated with the fluctuation displacement field $\tilde{\mathbf{u}}_{\mu_{ij}} \in \mathcal{V}_\mu$ that solves the linear variational problem

$$\int_{\Omega_\mu} \mathbb{C}_\mu \nabla^s \tilde{\mathbf{u}}_{\mu_{ij}} \cdot \nabla^s \boldsymbol{\eta} = -\int_{\Omega_\mu} \mathbb{C}_\mu (\mathbf{e}_i \otimes \mathbf{e}_j) \cdot \nabla^s \boldsymbol{\eta} \quad \forall \boldsymbol{\eta} \in \mathcal{V}_\mu, \tag{28}$$

for $i, j = 1, 2$ (in the two-dimensional case). In the above, $\{e_i\}$ denotes an orthonormal basis for the two-dimensional Euclidean space.

For a more detailed description on the derivation of expressions (25 – 28) we refer the reader to Michel et al. (1999); de Souza Neto and Feijóo (2006) and Giusti et al. (2009b).

4 EXPERIMENTAL PROCEDURE

The micrographs used in the research were obtained from 1-in Y-blocks (see Figure 4(a)) of slightly hypereutectic pearlitic nodular cast iron. The alloy used in the experiments was melted in a high frequency induction furnace of $15 \, kN$ capacity. The load consisted of: 23.26% SAE 1010 steel scrap, 23.26% nodular cast iron scrap, 6.6% pig iron, 41.8% of the puddle, to adjust the carbon content was employed 1.6% carbon (90% performance), 2.0% of steel sheets and steel shavings, 0.15% of SiCa and to adjust the silicon content was added Fe75%Si. The base metal was overheated to $1650°C$ for a period of about 20 minutes. Inoculation and nodularization treatments were carried out following the Sandwich Method, in which the substances are placed in a ladle and are covered with steel sheets and steel shavings, and then the liquid metal is poured from the furnace (Elliot, 2005). The treatment of the liquid was carried out with the addition of 1.5% FeSiMgCe (nodulizant) and 0.7% Fe75%Si (post-inoculation treatment). The molten metal was subsequently poured into the ladle to fill the Y-blocks. Then, the blocks were divided into 25 parts as shown in Figure 4(e).

The main elements of the chemical composition of the cast alloy are listed in Table 3.

Element	C	Si	Mn	P	S	Cr	Cu	Sn	Mg	CE
wt-%	3,55	2,78	0.49	0.012	0.010	0.023	0.89	0.010	0.054	4.52

Table 3: Average chemical composition (main elements) of samples, wt-%

The location of the five samples used in the analysis of the Y-blocks are shown in Figures 4(c), 4(d), and 4(e), and the points analyzed in each sample are indicated in Figure 4(c) and 4(d). The preparation of the samples consisted in the successive rough grinding using waterproof abrasive papers with grades ranging: 180, 240, 400, 600, 800 and 1000. Next, each sample was polished with diamond paste of granulometry of $6 \, \mu m$, and revealed with 2.2% of Nital. After that, the samples were observed under an optical microscope Olympus PMG 3 equipped with a video camera connected to a computer. The five micrographs were analyzed with image analysis software. Finally, the images were processed and analyzed for the five points of interest without nital attack.

The images corresponding to: original micrographs, segmented micrographs; original micrographs with lighting corrected and nodules contour detected and finite element mesh obtained with GMSH (Geuzaine and Remacle, 2009) are shown in Figure 6 to Figure 10, for some samples used in this work. Figure 11 shows some details of the finite element mesh used in simulations.

The metallurgical study consists in the determination of graphite and metal matrix volume fraction (the last is a mixture of ferrite and pearlite), and the graphite phase characterization which consists in the determination of size and roundness of each nodule and corresponding main and minor axis from the ellipse interpolated from each nodule. From the above measurements, the nodularity corresponding to each sample was calculated from (SinterCast, 1997):

$$Nodularity = \frac{\sum_{i=1}^{nodules} A_i + 0.5 \sum_{j=1}^{intermediates} A_j}{\sum_{k=1}^{nodules>10\mu m} A_k} 100 \tag{29}$$

(a) Two views of double 1in. Y-block mold.

(b) $3D$ view and cut's plane of 1in. Y-block

(c) Cut plane A. (d) Cut plane B. (e) Cut plane C.
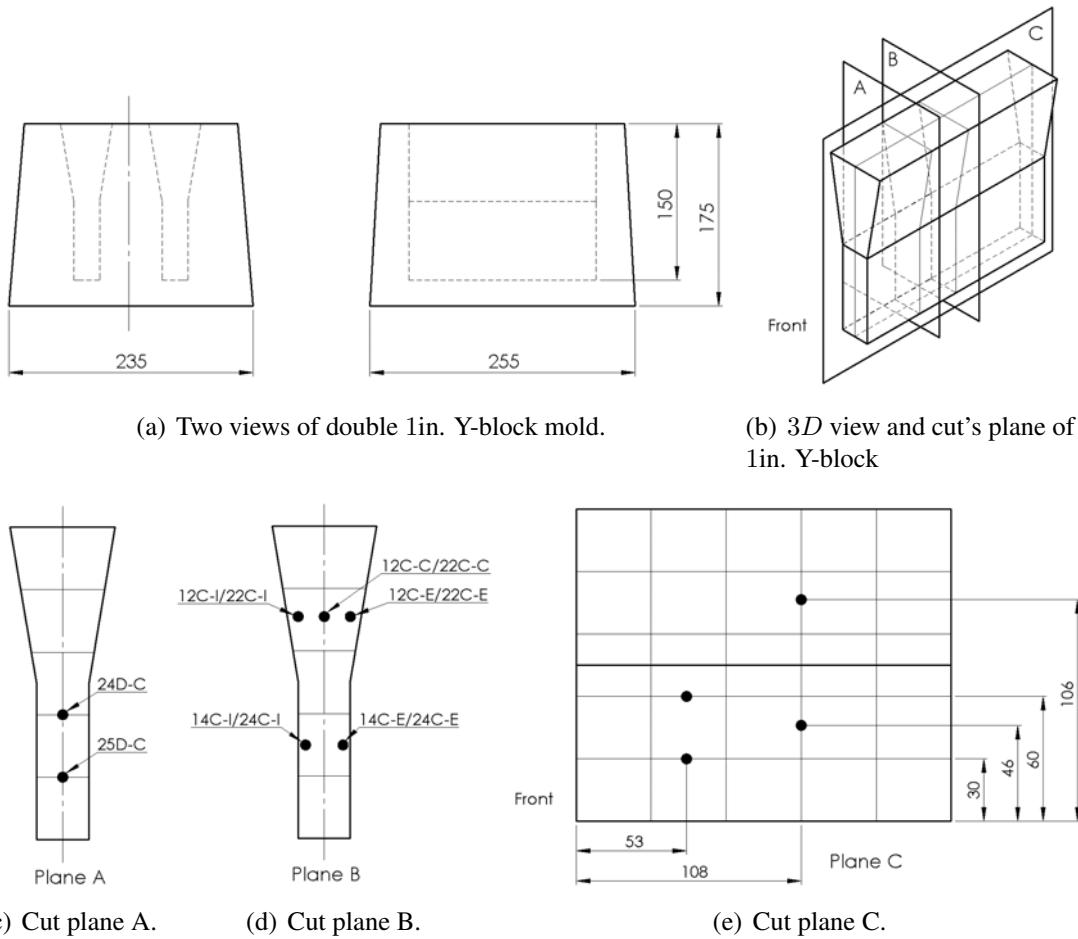
Figure 4: Mold, 1-in. Y-block and locations of the samples used for metallurgical study.

where A_i, A_j and A_k are, respectively, the surface areas of: *nodules* whose roundness is greater than 0.625, *intermediates* nodules whose roundness is greater than 0.525 and less than 0.625 (see Figure 5), and all nodules of the sample with diameter which is greater than $10\ \mu m$. In our case, the major axis of all nodules are greater than $10\ \mu m$. Note that the above expression is able to obtain the nodularity of the spheroidal graphite, for the case of compacted and flake graphite SinterCast (1997) and Sjogren (2007) adopts a negative nodularity.

Figure 5 shows the classification of graphite nodules according to roundness, which is calculated as follows (Castro et al., 2003):

$$Roundness = \frac{4\pi S}{P} \qquad (30)$$

where S and P are the surface and perimeter nodule, respectively.

For compacted graphite cast irons the nodularity is typically in the range of $0-10\%$, whereas that for spheroidal graphite cast iron the nodularity is approaching 100% and for flake graphite and according to SinterCast (1997) a nodularity of -5% describes a fully lamellar graphitic structure. The graphite Young's modulus varies as a function of nodularity according to (Sjogren, 2007):

$$E_i = 0.173 Nodularity + 18.9. \qquad (31)$$

Applying equation 31 for the case of spheroidal graphite cast iron with 100% nodularity, the graphite Young modulus is $36.2\ GPa$.

5 RESULTS AND DISCUSSION

The aim of this section is to present the obtained results from the multi-scale analysis and a comparison with the classical analytical expression of the Young's modulus for nodular cast-iron as mentioned in the previous section. The analytical expression in which this work is based is given by

$$
E_{eff} = E_m \left\{ 1 - \frac{\pi}{A} \left[1 - \frac{1}{9\left(1 + \frac{1.99}{B}\left\{\frac{E_m}{E_i} - 1\right\}\right)} - \frac{1}{3\left(1 + \frac{1.68}{B}\left\{\frac{E_m}{E_i} - 1\right\}\right)} \right. \right.
$$
$$
\left. \left. - \frac{5}{9\left(1 + \frac{1.04}{B}\left\{\frac{E_m}{E_i} - 1\right\}\right)} \right] \right\}, \tag{32}
$$

with

$$
A = \frac{\left(\frac{4\pi}{3c_i}\right)^{2/3} ar^{-1/3}}{\sqrt{1 + (ar^{-2} - 1)\cos^2\alpha_i}} \quad \text{and} \quad B = \left(\frac{4\pi}{3c_i}\right)^{1/3} ar^{1/3}\sqrt{1 + (ar^{-2} - 1)\cos^2\alpha_i} \tag{33}
$$

where E_{eff}, E_m, E_i are the modules of the cast iron, the matrix and the inclusion of graphite, respectively, and c_i is the volume fraction of the graphite, ar is the aspect ratio of the inclusions and $\cos^2\alpha_i$ describe the orientation of the inclusions. For the special case of random statistical orientation $\cos^2\alpha_i = 0.33$. A detailed explanation of this expression is given by Boccaccini (1997).

In the resolution of the set of variational problems eq.(28), for each multi-scale model described in Section 3.1, the numerical procedure described in Giusti et al. (2009a) was used. The parameters that describe the material properties of the matrix and graphite phases are presented in Table 4. In all cases the finite element mesh used was build with triangular linear elements. The elements and nodes obtained for each mesh are shown in Table 5, and Figures 6 to 10.

The results obtained from the multi-scale simulation and the analytical expression described above are presented in Table 6. In Figures12 and 13 the Young's modulus obtained from the
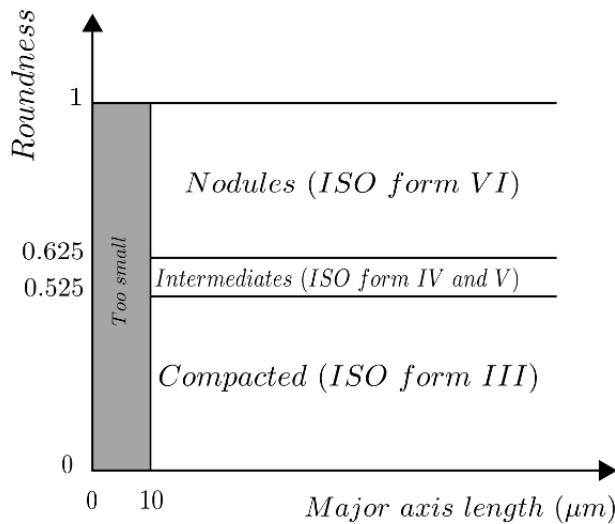


Figure 5: Classification of graphite nodules according to roudness (SinterCast, 1997).

| (a) Original | (b) Segmented | (c) Nodule contours | (d) FEM mesh |
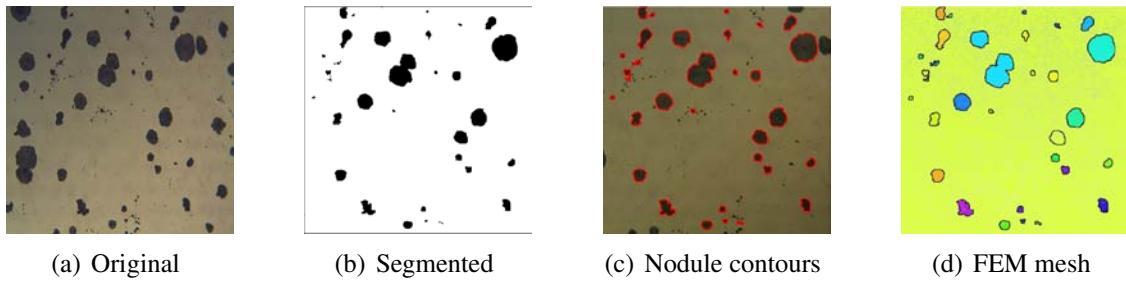
Figure 6: Images corresponding to $14C \times 100\_E$ sample (see Figure 4(d))

| (a) Original | (b) Segmented | (c) Nodule contours | (d) FEM mesh |
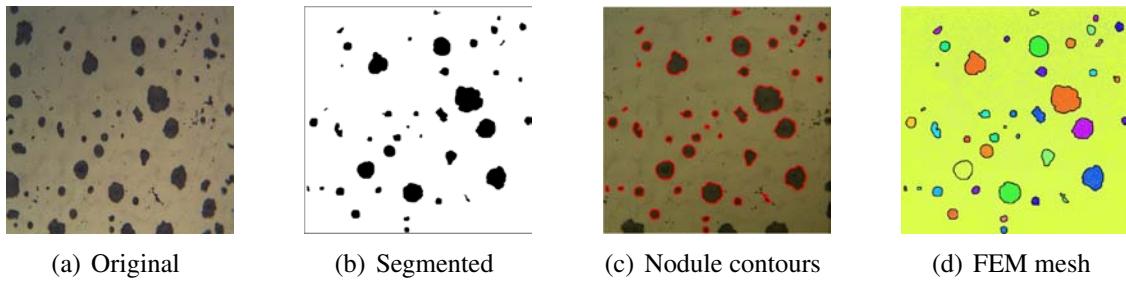
Figure 7: Images corresponding to $14C \times 100\_I$ sample (see Figure 4(d))

| (a) Original | (b) Segmented | (c) Nodule contours | (d) FEM mesh |
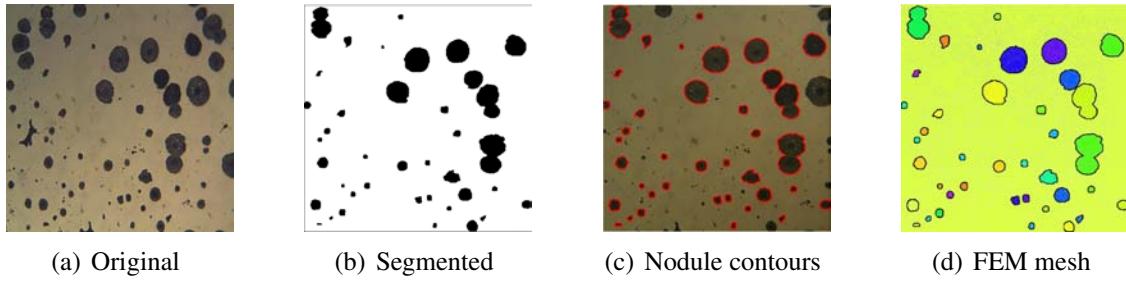
Figure 8: Images corresponding to $22C \times 100\_C$ sample (see Figure 4(d))

| (a) Original | (b) Segmented | (c) Nodule contours | (d) FEM mesh |
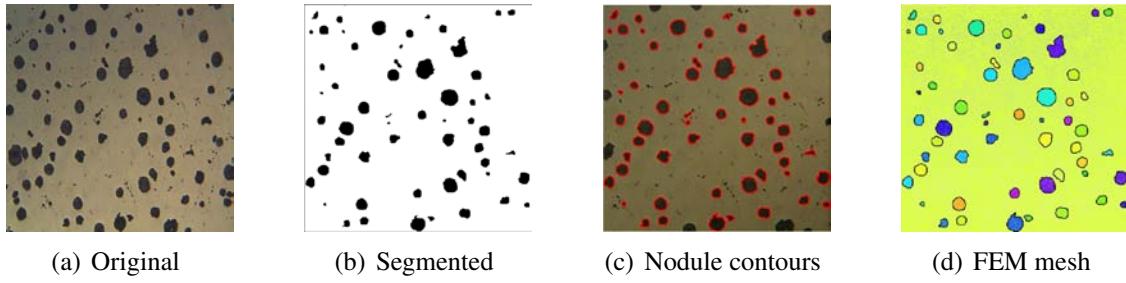
Figure 9: Images corresponding to $22C \times 100\_E$ sample (see Figure 4(d))

different methodologies described previously are plotted as a function of the graphite volume fraction and the nodularity, respectively.

From the above results, it is clear that the rule of mixture model provides the most rigid constitutive response and the uniform boundary traction model gives the least rigid behavior of the material, as predicted by the theory presented in Section 3.1. On the other hand, the behavior predicted by eq.(32) gives a Young's modulus very close to the Linear multi-scale model with an average difference around 1.23%. For the other multi-scale models the average difference are of 1.68% (periodic model) and 2.60% (uniform traction model). In the cases analyzed, the

(a) Original   (b) Segmented   (c) Nodule contours   (d) FEM mesh
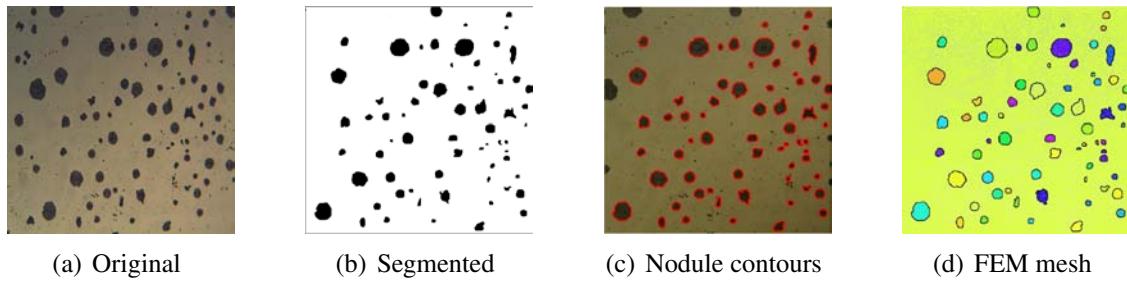
Figure 10: Images corresponding to $22C \times 100\_I$ sample (see Figure 4(d))
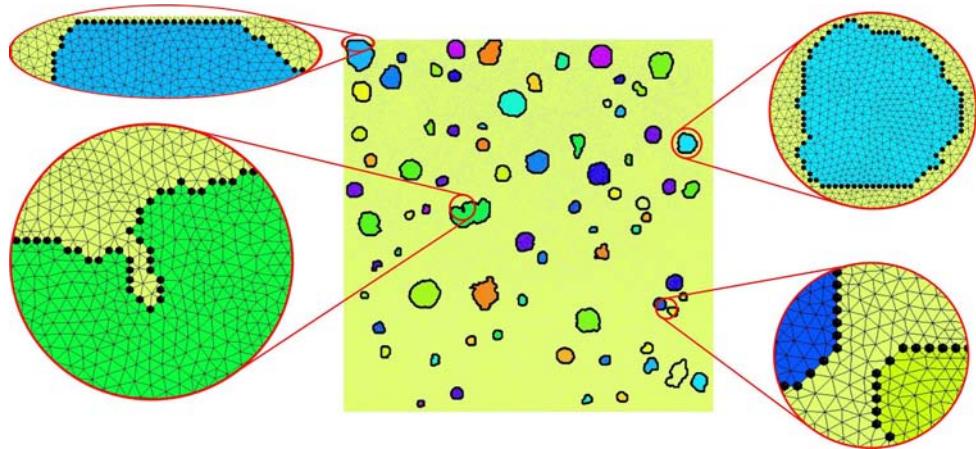
Figure 11: Mesh details for sample $12C \times 100\_C$.

Sample	Graphite vol. frac. (c_i)	Aspect ratio (as)	Nodularity %	Young's Modulus		Poisson ratio	
				E_m	E_i	Matrix	Graphite
12Cx100_C	9.904	0.827	94.529	206	35.254	0.290	0.2225
12Cx100_E	7.728	0.834	98.047	206	35.862	0.290	0.2225
12Cx100_I	7.653	0.862	99.018	206	36.030	0.290	0.2225
14Cx100_E	7.247	0.736	88.275	206	34.172	0.290	0.2225
14Cx100_I	8.252	0.799	94.114	206	35.182	0.290	0.2225
22Cx100_C	11.605	0.852	88.049	206	34.133	0.290	0.2225
22Cx100_E	9.183	0.835	97.359	206	35.743	0.290	0.2225
22Cx100_I	8.898	0.824	95.765	206	35.467	0.290	0.2225
24Cx100_E	8.043	0.776	92.581	206	34.916	0.290	0.2225
24Cx100_I	8.328	0.758	98.405	206	35.924	0.290	0.2225
24Dx100	7.703	0.797	97.223	206	35.721	0.290	0.2225
25Dx100	11.905	0.819	97.542	206	35.775	0.290	0.2225

Table 4: Constitutive properties of the phases used in the simulations. Young's Modulus in GPa.

difference does not exceed the value of 5%. When the effective modulus is compared versus the nodularity of the samples, Figure 13, each model has the same behavior as the analytical eq.(32). This fact has the origin in the linearity of the expression for the Young's modulus of the graphite with the nodularity, see eq.(31). In addition, note that the variation of the effective modulus with the nodularity and the aspect ratio of the graphite inclusion are very small. For example, for a variation of the 14.62% in the aspect ratio and of 11.08% in the nodularity of the

Sample	Elements	Nodes
12Cx100_C	406900	204477
12Cx100_E	421760	211907
12Cx100_I	406940	204497
14Cx100_E	431388	216721
14Cx100_I	424174	213114
22Cx100_C	409826	205940
22Cx100_E	411134	206594
22Cx100_I	415094	208574
24Cx100_E	426040	214047
24Cx100_I	428000	215027
24Dx100	409552	205803
25Dx100	410132	206093

Table 5: Elements and nodes for the meshes.

Sample	Graphite vol. frac. (c_i)	Nodularity %	Young's Modulus [GPa]				
			Taylor	Linear	Periodic	Uniform	eq.32
12Cx100_C	9.904	94.529	189.089	172.606	171.639	169.617	174.686
12Cx100_E	7.728	98.047	192.852	179.480	178.709	177.176	180.252
12Cx100_I	7.653	99.018	192.992	179.838	179.449	178.632	180.082
14Cx100_E	7.247	88.275	193.548	180.195	179.410	177.042	182.629
14Cx100_I	8.252	94.114	191.904	177.014	176.761	175.856	179.280
22Cx100_C	11.605	88.049	186.055	166.455	165.123	162.487	169.613
22Cx100_E	9.183	97.359	190.365	174.187	173.553	172.483	176.477
22Cx100_I	8.898	95.765	190.826	175.770	175.295	174.296	177.308
24Cx100_E	8.043	92.581	192.240	177.621	176.887	175.559	180.138
24Cx100_I	8.328	98.405	191.836	177.235	176.391	174.748	180.058
24Dx100	7.703	97.223	192.884	179.019	178.104	176.206	180.862
25Dx100	11.905	97.542	185.735	166.601	165.486	164.003	170.271

Table 6: Results for the different models analized.

samples, the obtained differences in the effective modulus are the same as mentioned above.

This indicates that the volume fraction is the most important characteristic for this type of composite. Other characteristics of composites of this type, such as nodularity, sphericity, aspect ratio, proximity and distribution of the graphite inclusions, provide a second-order effect in the Young's modulus and can be neglected in an engineering application of these materials. However, the characteristics previously mentioned have a very important role in the inelastic behavior of the material and deserve a careful attention in a multi-scale study.

6 CONCLUSIONS

A comparison between a classical analytical expression for the effective Young's modulus and the results of a computationally-based multi-scale analysis has been presented in this paper. For an adequate definition of the RVE, a set of micrographic images obtained from an optical device was used. Each image was enhanced and segmented to obtain the volume fraction of each phase and the boundary of each object in the micrograph. With this information, a finite
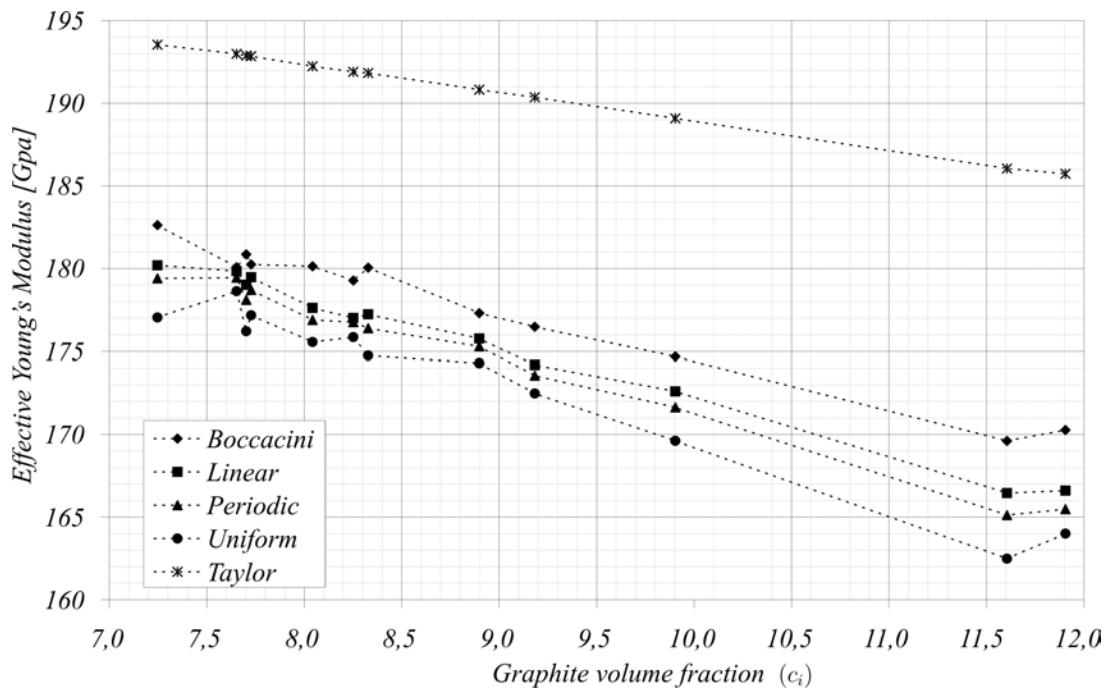
Figure 12: Comparison of the results of multi-scale simulation and analytical expression.
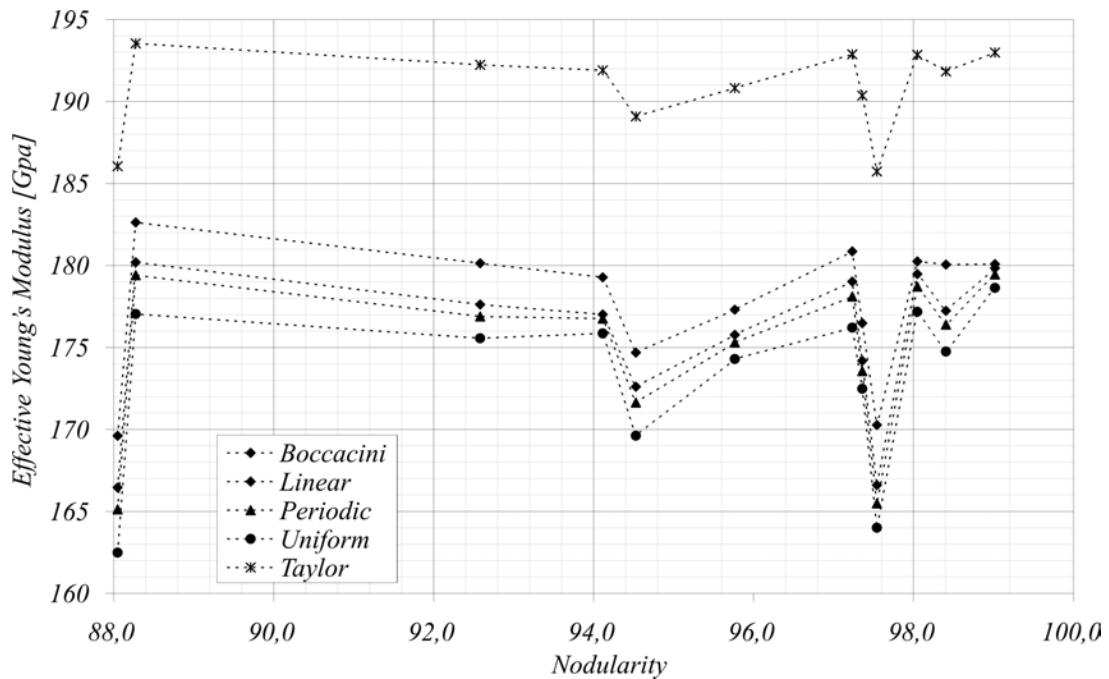
Figure 13: Comparison of the results of multi-scale simulation and analytical expression.

element mesh was constructed, for each image, using a open-source software. The multi-scale model is based in a classical homogenization procedure over a variational framework. For this work, only the linear elasticity model was used in the derivation of the macroscopic Young's modulus. The results obtained indicate a good match of the analytical expression with the classical linear boundary displacement multi-scale model. For the other models investigated, the difference never exceeded the 5%. This difference indicates that the analytical expression given by eq.(32) can be used in an engineering application in the prediction of the effective

elastic parameter. However, for an accurate estimate of the macroscopic Young's modulus, a more detailed multi-scale study is needed. In particular, it is necessary take into account, among others, the shape and size of the RVE. These aspects are currently under investigation.

ACKNOWLEDGEMENTS

REFERENCES

ASTM A247. Standard test method for evaluating the microstructure of graphite in iron castings. 1998.

ASTM A536. Standard specification for ductile iron castings. 2009.

Bensoussan A., Lions J., and Papanicolau G. *Asymptotic analysis for periodic microstructures*. North Holland, Amsterdam, 1978.

Boccaccini A.R. Effect of graphite inclusions on the young's modulus of cast iron. *Zeitschrift für METALLKUNDE*, 88(1):23–26, 1997.

Castro M., Herrera-Trejo M., Alvarado-Reyna J.L., Martínez-Tello C.L., and Méndez-Nonell M. Characterization of graphite form in nodular graphite cast iron. *International Journal of Cast Metals Research*, 16(1-3):83–86, 2003.

Collini L. and Nicoletto G. Determination of the relationship between microstructure and constitutive behaviour of nodular cast iron with a uni cell model. *The Journal of Strain Analysis for Engineering Design*, 40(2):95–106, 2005.

de Souza Neto E. and Feijóo R. Variational foundations of multi-scale constitutive models of solid: small and large strain kinematical formulation. Technical Report No 16/2006, Laboratório Nacional de Computação Científica LNCC/MCT, Petrópolis, Brasil, 2006.

Elliot R. *Cast Iron Technology*. Jaico Publishing House, 2005.

Germain P., Nguyen Q., and Suquet P. Continuum thermodynamics. *Journal of Applied Mechanics, Transactions of the ASME*, 50(4):1010–1020, 1983.

Geuzaine C. and Remacle J.F. Gmsh: a three-dimensional finite element mesh generator with built-in pre- and post-processing facilities. *International Journal for Numerical Methods in Engineering*, 79(11):1309–1331, 2009.

Giusti S., Blanco P., de Souza Neto E., and Feijóo R. An assessment of the Gurson yield criterion by a computational multi-scale approach. *Engineering Computations*, 26(3):281–301, 2009a.

Giusti S., Novotny A., de Souza Neto E., and Feijóo R. Sensitivity of the macroscopic elasticity tensor to topological microstructural changes. *Journal of the Mechanics and Physics of Solids*, 57(3):555–570, 2009b.

Guo X., Stefanescu D.M., Chuzhoy L., Pershing M.A., and Biltgen G.L. A mechanical properties model for ductile iron. *AFS Transactions*, 105:47–54, 1997.

Hill R. A self-consistent mechanics of composite materials. *Journal of the Mechanics and Physics of Solids*, 13(4):213–222, 1965.

Lundback E., Svensson I.L., and Person P. Modelling of structure formation and relation to mechanical properties of nodular cast iron. In J.L. Chenot and E. Oñate, editors, *Modelling of metal forming processes: proceedings of the Euromech 233 Colloquium*, pages 37–46. Dordrecht: Kluwer, cop., Sophia Antipolis, France, 1988.

Mandel J. *Plasticité classique et viscoplasticité*. CISM Lecture Notes. Springer-Verlag, Udine, 1971.

Mazilu P. and Ondracek G. On the effective young's modulus of elasticity for porous materials. part i: The general model equation. In K. Herrmann and Z. Olesiak, editors, *Thermal effects in fracture of multiphase materials. Proceedings of Euromechanic 255 Colloquium*, pages 214–255. Springer-Verlag, Paderborn, FRG, 1990.

Michel J., Moulinec H., and Suquet P. Effective properties of composite materials with periodic microstructure: a computational approach. *Computer Methods in Applied Mechanics and Engineering*, 172(1-4):109–143, 1999.

Miehe C., Schotte J., and Schröder J. Computational micro-macro transitions and overall moduli in the analysis of polycrystals at large strains. *Computational Materials Science*, 16(1-4):372–382, 1999.

Nicoletto G., Collini L., Konecná, and Riva E. Analysis of nodular cast iron microstructures for micromechanics model development. *Strain*, 42(2):89–96, 2006.

Panchal S. Indian foundry industry. 2010.

Pundale S.H., Rogers R.J., and Nadkarni G.R. Finite element modeling of elastic modulus in ductile irons: Effect of graphite morphology. *AFS Transactions*, 102(98):99–105, 2000.

Sanchez-Palencia E. *Non-homogeneous media and vibration theory*, volume 127 of *Lecture Notes in Physics 127*. Springer-Verlag, Berlin, 1980.

SinterCast. *SinterCast Nodularity Rating Chart*. SinterCast, 1997.

Sjogren T. *Influences of the graphite phase on elastic and plastic deformation behaviour of cast irons*. Ph.D. thesis, INSTITUTE OF TECHNOLOGY, Department of Management and Engineering, Division of Engineering Materials, Linköping University, Jönköping, Sweden, 2007.

Spada A., Rajan C., and Gil P. U.s. ductile iron metalcasting: Competing globally. In K.L. Hayrynen, editor, *Proceedings of the Keith Millis Symposium on Ductile Cast Iron*, pages 4–5. DIS AFS, Las Vegas, Nevada, USA, 2008.

Svensson I.L., Wessen M., and Gonzáles A. Modeling of structure and hardness in nodular cast iron castings at different silicon contents. In *Proceedings of Modeling of Castings: Welding and Advanced Solidification Process VI*, pages 29–36. Minerals, Metals and Materials Society (TMS, Warrendale, PA), Palm Coast, Florida, USA, 1993.

Venugopalan D. and Alagarsamy A. Effects fo alloy adittions on the microstructure and mechanical properties of commercial ductile iron. *AFS Transactions*, 98:395–400, 1990.

Wenzhen L. and Baicheng L. Microstructure simulation and properties prediction of spheroidal graphite iron castings. In *Proceedings of* 62*ND WORLD FOUNDRY CONGRESS*. Philadelphia, Pennsylvania, USA, 1996.

Wolfgang G., Roland M., Ulrich W., and Siegfried S. Self-consistent one-particle 3d unit cell model for simulation of the effect of graphite aspect ratio on youngs's modulus of cast iron. *Computational Materials Science*, 28(3-4):654–662, 2003.

Yu S.K. and Loper Jr. C.R. The effect of molybdenum, copper and nickel on the pearlitic and martensitic hardenability of ductile cast irons. *AFS Transactions*, 96:811–822, 1988.